

ON A MONOTONE SCHEME FOR NONCONVEX NONSMOOTH OPTIMIZATION WITH APPLICATIONS TO FRACTURE MECHANICS

DARIA GHILLI AND KARL KUNISCH

ABSTRACT. A general class of nonconvex optimization problems is considered, where the penalty is the composition of a linear operator with a nonsmooth nonconvex mapping, which is concave on the positive real line. The necessary optimality condition of a regularized version of the original problem is solved by means of a monotonically convergent scheme. Such problems arise in continuum mechanics, as for instance cohesive fractures, where singular behaviour is usually modelled by nonsmooth nonconvex energies. The proposed algorithm is successfully tested for fracture mechanics problems. Its performance is also compared to two alternative algorithms for nonsmooth nonconvex optimization arising in optimal control and mathematical imaging.

Nonsmooth nonconvex optimization and monotone algorithm and fracture mechanics and sparse recovery

1. INTRODUCTION

In this paper we investigate a class of nonconvex and nonsmooth optimization problems, where the penalty is the composition of a nonsmooth nonconvex mapping with a linear operator and the smooth part is a least squares type term.

Similar optimization problems in the case where the operator inside the penalty coincides with the identity matrix have attracted increasingly attention due to their applications to sparsity of solutions, feature selection, and many other related fields as e.g. compressed sensing, signal processing, and machine learning (see e.g. [8, 12]). The convex nonsmooth case of the ℓ^1 norm has gained large popularity and has been thoroughly studied. The convexity allows to formulate efficient and globally convergent algorithms to find a numerical solution. Here we mention [11, 39] where the basis pursuit and the Lasso problems were introduced to solve ℓ^1 minimization problems.

Recently increased interest has arisen towards nonconvex and nonsmooth penalties, such as the ℓ^τ quasi-norm, with τ larger or equal to zero and less than 1 (see e.g. [6, 24, 27, 30, 32, 35]), the smoothly clipped absolute deviation (SCAD) [16, 29], and the minimax concave penalty (MCP) [40, 29]. The nonconvexity has been shown to provide some advantages with respect to the convex models. For example, it allows to require less data in order to recover exactly the solution (see e.g. [10, 18, 37]) and it tends to produce unbiased estimates for large coefficients [41, 16, 17]. Note that all the previously mentioned works deal with the particular case where the operator coincides with the identity.

Nonconvex optimization problems as we consider, where the operator inside the penalty is different from the identity, arise also in the modelling of cohesive fractures in continuum mechanics, where the concavity of the penalty is crucial to model the evolution of the fracture energy released within the growth of the crack opening. Here the operator is of importance

This work was supported by the ERC advanced grant 668998 (OCLOC) under the EU's H2020 research programme.

to model the jump of the displacement between the two lips of the fractures. We refer to [34, 20, 1, 2] and subsection 3.1 for more details.

The study of these problems for nonconvex penalties, including ℓ^τ , with τ strictly positive and less than 1, the SCAD and the MCP functionals, and for linear operators not necessarily coinciding with the identity, is also motivated by applications different from those arising in fracture mechanics. For example in imaging the ℓ^τ quasi-norm, with τ strictly positive and less than 1, of the numerical gradient of the solution has been proposed as a nonconvex extension of the total variation (like TV) regularizer (see e.g [24, 35]) in order to reconstruct piecewise smooth solutions. The SCAD and the MCP penalties have been used for high dimensional regression and variable selection methods in high-throughput biomedical studies [7]. We mention also that the SCAD has been proposed as a nonconvex penalty in the network estimation to attenuate the bias problem [15].

The main difficulties in the analysis of these problems come from the interplay between the nonsmoothness, the nonconvexity, and the coupling between coordinates which is described by the operator inside the penalty. Since standard algorithms are not readily available, the resolution of these problems requires the development of new analytical and numerical techniques.

In the present paper we propose a monotonically convergent algorithm to solve this kind of problems. This is an iterative procedure which solves the necessary optimality condition of a regularized version of the original problem. A remarkable property of our scheme is the strict monotonicity of the functional along the sequence of iterates. The convergence of the iteration procedure is proved under the same assumptions that guarantee existence of solutions.

The performance of the scheme is successfully tested to simulate the evolution of cohesive fractures for several different test configurations. Then we turn to an issue of high relevance, namely the comparison between two alternative algorithms, the GIST "General Iterative Shrinkage and Thresholding" algorithm for ℓ^τ minimization, with τ strictly positive and less than 1 and the FISTA "Fast Iterative Shrinkage-Thresholding Algorithm" for ℓ^1 minimization. The comparison is carried out with respect to the infimal value reached by the iteration procedure and with respect to computing time. Our results show that the monotone algorithm is able to reach a smaller value of the objective functional that we consider when compared to the one of GIST. Note that, differently from GIST, the monotone scheme solves a system of nonlinear equations at each iteration level. We remark that in [33] GIST was compared with the IRLS "iterative reweighted least squares" algorithm, which is another popular scheme for ℓ^τ minimization, with τ strictly positive and less than 1. The results of [33] show that GIST and IRSL have nearly the same performance, with only one difference which is speed, where GIST appears to be the faster one.

An analogous procedure to the one proposed in the present paper was developed in [20] to solve similar problems where the nonconvex penalty coincides with ℓ^τ quasi-norm, with τ strictly positive and less than or equal to 1. With respect to [20], in the present paper we deal with more general concave penalties. Moreover, we carry out several numerical experiments for diverse situations in cohesive fracture mechanics, comparing the behaviours for different concave penalties such as the SCAD, the MCP and the ℓ^τ penalty, with τ strictly positive and less than 1. Finally in the present paper we compare the performance of the scheme with that of GIST.

Let us recall some further literature concerning nonconvex nonsmooth optimization of the type investigated in the present paper. In [29, 28] a primal-dual active set type algorithm has been developed, in the case the operator inside the penalty coincides with the identity. For more references in this case we refer to [20]. Concerning ℓ^τ minimization, with τ larger than or equal to zero and less than or equal to 1 when the operator is not the identity, other techniques have recently been investigated. Here we mention iteratively reweighted convex majorization

algorithms [35], alternating direction method of multiplier (ADMM) [32] and finally a Newton-type solution algorithm for a regularized version of the original problem [24]. Finally we recall the paper [1], where a novel algorithm for nonsmooth nonconvex optimization with linear constraints is proposed, consisting of a generalization of the well-known nonstationary augmented Lagrangian method for convex optimization. The convergence to critical points is proved and several tests were made for free-discontinuity variational models, such as the Mumford-Shah functional. The nonsmoothness considered in [1] does not allow singular behaviour of the type that the ℓ^τ term, with τ larger than or equal to zero and strictly less than 1 does.

The paper is structured as follows. In Section 2, subsection 2.1 we state the precise assumptions, in subsection 2.2 we prove existence for the problem in consideration, in subsection 2.3 we propose the monotone scheme to solve a regularized version of the original problem and we prove its convergence, and finally in subsection 2.4 we study the asymptotic behavior as the concavity and regularization parameters go to zero. In Section 3 we present the precise form of our scheme. In subsection 3.1 we discuss our numerical experience for cohesive evolution of fracture mechanics and in subsection 3.2 we compare the performance of our scheme to that of GIST for three different test cases, the academical M-matrix example, an optimal control problem and a microscopy imaging example.

2. EXISTENCE AND MONOTONE ALGORITHM

2.1. Assumptions. We consider

$$(2.1) \quad \min_{x \in \mathbb{R}^n} J(x) = \frac{1}{2} \|Ax - b\|_2^2 + \sum_{i=1}^r \phi(\Lambda x)_i,$$

where $A \in \mathbb{M}^{m \times n}$, $\Lambda \in \mathbb{M}^{r \times n}$, $b \in \mathbb{R}^m$ and $\phi(t) : \mathbb{R} \rightarrow \mathbb{R}^+$ satisfies

$$(\mathbf{H}) \quad \begin{cases} \text{(i)} & \phi \text{ is even with } \phi(0) = 0, \text{ nondecreasing for } t \geq 0 \text{ and continuous;} \\ \text{(ii)} & \phi \text{ is differentiable on }]0, \infty[; \\ \text{(iii)} & \phi \text{ is concave on } \mathbb{R}^+; \\ \text{(iv)} & \text{there exists a neighbourhood of zero where the function } t \rightarrow \frac{\phi'(t)}{t} \text{ is monotone;} \end{cases}$$

Above monotonically increasing or decreasing are admitted. Throughout the rest of the paper we will use the notation

$$\Phi(\Lambda x) := \sum_{i=1}^r \phi(\Lambda x)_i.$$

Under assumption **(H)**, the following two cases are analysed:

- (a) (i) $\phi(t)$ is a constant when $|t| \geq t_0$ for some $t_0 > 0$;
(ii) A is coercive, i.e. $\text{rank}(A) = n$.
- (b) (i) for some $\gamma > 0$ it holds $\phi(at) = a^\gamma \phi(t)$ for all $t \in \mathbb{R}$ and $a \in \mathbb{R}^+$;
(ii) $\text{Ker}(A) \cap \text{Ker}(\Lambda) = \{0\}$.

Three popular examples of nonconvex penalties which satisfy **(H)** and the assumptions on ϕ in (a) or (b) are the following:

ℓ^τ : $\tau \in (0, 1], \lambda > 0$

$$(2.2) \quad \phi(t) = \lambda |t|^\tau,$$

satisfying **(b)(i)**.

SCAD: $\tau > 1, \lambda > 0$

$$(2.3) \quad \phi(t) = \begin{cases} \frac{\lambda^2(\tau+1)}{2} & |t| \geq \lambda\tau \\ \frac{\lambda\tau|t| - \frac{1}{2}(t^2 + \lambda^2)}{\tau-1} & \lambda < |t| \leq \lambda\tau \\ \lambda|t| & |t| \leq \lambda, \end{cases}$$

satisfying (a)(i).

MCP: $\tau > 1, \lambda > 0$

$$(2.4) \quad \phi(t) = \begin{cases} \lambda(|t| - \frac{t^2}{2\lambda\tau}) & |t| < \lambda\tau \\ \frac{\lambda^2\tau}{2} & |t| \geq \lambda\tau, \end{cases}$$

satisfying (a)(i).

Remark 2.1. The singularity at the origin of the three penalties leads to sparsity of the solution. In the SCAD and the MCP, the derivative vanishes for large values to ensure unbiasedness.

Problems as (2.1) with ϕ given by the ℓ^τ -quasi norm with $\tau \in (0, 1)$ were studied in [20]. For more details on its statistical properties, such as variable selection and oracle property, of the ℓ^τ -quasi norm, we refer to [10, 18, 25, 31].

The SCAD (smoothly clipped absolute deviation) ([16, 17]) has raised interest in relation to variable selection consistency and asymptotic estimation efficiency (see [17]). It can be obtained upon integration of the following formula for $\tau > 2$

$$\phi(t) = \lambda \int_0^{|t|} \min\left(1, \frac{\max(0, \lambda\tau - |s|)}{\lambda(\tau - 1)}\right) ds.$$

The MCP (minimax concave penalty) [40] can be recovered from the following formula

$$\phi(t) = \lambda \int_0^{|t|} \max\left(0, 1 - \frac{|s|}{\lambda\tau}\right) ds$$

and minimizes the maximum concavity $\sup_{0 < t_1 < t_2} \frac{(\phi'(t_1) - \phi'(t_2))}{(t_2 - t_1)}$ subject to the constraints $\phi'(t) = 0$ for any $|t| \geq \lambda\tau$ (unbiasedness) and $\phi'(0^\pm) = \pm\lambda$ (feature selection). The condition $\tau > 1$ ensures the wellposedness of the thresholding operator.

2.2. Existence. First we prove coercivity of the functional J in (2.1) under assumptions (a) or (b).

Lemma 2.1. *Let assumptions **(H)** and either (a) or (b) hold. Then the functional J in (2.1) is coercive.*

Proof. Under assumption (a), the coercivity of J follows trivially. Suppose now that (c) holds. Then the result follows by similar arguments to that used in [20], Theorem 1 (where ϕ is the ℓ^τ quasi-norm). We proceed by contradiction and we suppose that $|x_k|_2 \rightarrow +\infty$ and $J(x_k)$ is bounded. For each k , let $x_k = t_k z_k$ be such that $t_k \geq 0, x_k \in \mathbb{R}^n$ and $|z_k|_2 = 1$. By (b) (i) we have

$$\Phi(\Lambda z_k) = \frac{1}{t_k^\gamma} \Phi(\Lambda x_k)$$

and then since $t_k \rightarrow +\infty$ and $J(x_k)$ is bounded, we have for $k \rightarrow +\infty$

$$0 \leq |Az_k|_2^2 + \Phi(\Lambda z_k) = \frac{1}{t_k^2} |Ax_k|_2^2 + \frac{1}{t_k^\gamma} \Phi(\Lambda x_k) \leq \frac{1}{t_k^{\min\{2, \gamma\}}} (|Ax_k|_2^2 + \Phi(\Lambda x_k)) \rightarrow 0$$

and hence

$$\lim_{k \rightarrow +\infty} |Az_k|_2^2 + \Phi(\Lambda z_k) = 0.$$

By compactness, the sequence $\{z_k\}$ has an accumulation point \bar{z} such that $|\bar{z}| = 1$ and $\bar{z} \in \text{Ker}(A) \cap \text{Ker}(\Lambda)$, which contradicts (c) (ii). \square

In the following theorem we state the existence of at least a minimizer to (2.1) under either (a) or (b). We omit the proof since it follows directly by the continuity and coercivity of the functional in (2.1).

Theorem 2.2. *Let assumptions **(H)** and either (a) or (b) hold. Then there exists at least one minimizer to problem (2.1).*

Remark 1. We remark that when assumption (a) (i) holds but A is not coercive, existence can still be proven in case $\Lambda \in \mathbb{R}^{n \times n}$ is invertible. Indeed by the invertibility of Λ , one can define $\bar{y} = \Lambda^{-1}\bar{x}$, where \bar{x} is a minimizer of $\bar{J}(x) = \frac{1}{2}|(A\Lambda^{-1})x - b|_2^2 + \Phi(x)$ and prove that \bar{y} is a minimizer of (2.1). The existence of a minimizer for the functional \bar{J} was proven in [28], Theorem 2.1.

However in our analysis we cover the two cases (a) and (b) since when (a) (ii) is replaced by the invertibility of Λ , we can not prove the coercivity of J , which is a key element for the convergence of the algorithm that we analyse (see the following section).

2.3. A monotone convergent algorithm. Following [27], in order to overcome the singularity of the function $\phi(t)$ near $t = 0$, we consider for $\varepsilon > 0$ the following regularized version of (2.1)

$$(2.5) \quad \min_{x \in \mathbb{R}^n} J_\varepsilon(x) = \frac{1}{2}|Ax - b|_2^2 + \Psi_\varepsilon(|\Lambda x|^2),$$

where for $t \geq 0$

$$(2.6) \quad \Psi_\varepsilon(t) = \begin{cases} \frac{\phi'(\varepsilon)}{2\varepsilon}t + \left(1 - \frac{\phi'(\varepsilon)\varepsilon}{2\phi(\varepsilon)}\right)\phi(\varepsilon) & \text{for } 0 \leq t \leq \varepsilon^2 \\ \phi(\sqrt{t}) & \text{for } t \geq \varepsilon^2, \end{cases}$$

and $\Psi_\varepsilon(|\Lambda x|^2)$ is short for $\sum_{i=1}^r \Psi_\varepsilon(|(\Lambda x)_i|^2)$. Note that

$$(2.7) \quad \Psi'_\varepsilon(t) = \frac{1}{\max\left\{\frac{2\varepsilon}{\phi'(\varepsilon)}, \frac{2\sqrt{t}}{\phi'(\sqrt{t})}\right\}} \geq 0 \quad \text{on } (0, \infty),$$

hence Ψ_ε is C^1 and by assumption **(H)** (iii) is concave on $[0, \infty)$. Moreover $t \rightarrow \Psi_\varepsilon(t^2) \in C^1(-\infty, \infty)$.

Remark 2. In (2.7) we suppose that the function $x \rightarrow \frac{\phi'(x)}{x}$ is decreasing. When the function $x \rightarrow \frac{\phi'(x)}{x}$ is increasing, one needs to replace the maximum in (2.7) with the minimum and the following results follow as well.

The necessary optimality condition for (2.5) is given by

$$(2.8) \quad A^*Ax + \Lambda^* \frac{1}{\max\left\{\frac{\varepsilon}{\phi'(\varepsilon)}, \frac{|\Lambda x|}{\phi'(|\Lambda x|)}\right\}} \Lambda x = A^*b,$$

the second addend is short for the vector with l -component $\sum_{i=1}^r (\Lambda^*)_{li} \frac{1}{\max\left\{\frac{\varepsilon}{\phi'(\varepsilon)}, \frac{|\Lambda x|}{\phi'(|\Lambda x|)}\right\}} (\Lambda x)_i$.

For convenience of exposition in the following we write (2.8) in the more compact notation

$$A^*Ax + 2\Lambda^*\Psi'_\varepsilon(|\Lambda x|^2)\Lambda x = A^*b,$$

where the l -component of the second addend is given by $\sum_{i=1}^r (\Lambda^*)_{li} \Psi'_\varepsilon(|(\Lambda x)_i|^2) (\Lambda x)_i$.

This can equivalently be expressed as

$$(2.9) \quad A^*Ax + 2\Lambda^*\Psi'_\varepsilon(|y|^2)y = A^*b \quad \text{with } y = \Lambda x.$$

In order to solve (2.9), the following iterative procedure is considered:

$$(2.10) \quad A^*Ax^{k+1} + 2\Lambda^*\Psi'_\varepsilon(|y^k|^2)y^{k+1} = A^*b \quad \text{where } y^k = \Lambda x^k.$$

Existence of a solution to equation (2.10) for any $k \geq 0$ follows from the existence of a minimizer of the associated optimization problem

$$(2.11) \quad \min_{x \in \mathbb{R}^n} \frac{1}{2}|Ax - b|_2^2 + \left| \sqrt{\Psi'_\varepsilon(|y^k|^2)}\Lambda x \right|_2^2.$$

We have the following convergence result.

Theorem 2.3. *Assume **(H)** and either (a) or (b). For $\varepsilon > 0$, let $\{x_k\}$ be generated by (2.10). Then $J_\varepsilon(x_k)$ is strictly monotonically decreasing, unless there exists some k such that $x^k = x^{k+1}$, and x^k satisfies the necessary optimality condition (2.9). Moreover every cluster point of x^k , of which there exists at least one, is a solution of (2.9).*

Proof. The proof strongly depends on the coercivity of the functional J and it follows arguments similar to those of [27, Theorem 4.1].

Multiplying (2.10) by $x^{k+1} - x^k$, we get

$$(2.12) \quad \begin{aligned} \frac{1}{2}|Ax^{k+1}|^2 - \frac{1}{2}|Ax^k|^2 + \frac{1}{2}|A(x^{k+1} - x^k)|^2 &+ (2\Psi'_\varepsilon(|y^k|^2)y^{k+1}, y^{k+1} - y^k) \\ &= (A^*b, x^{k+1} - x^k). \end{aligned}$$

Note that

$$(2.13) \quad (y^{k+1}, y^{k+1} - y^k) = \frac{1}{2} \sum_{i=1}^n (|y_i^{k+1}|^2 - |y_i^k|^2 + |y_i^{k+1} - y_i^k|^2).$$

By assumption **(H)** (iii) the function $t \rightarrow \Psi_\varepsilon(t)$ is concave on $[0, \infty)$, and we have

$$(2.14) \quad 2\Psi_\varepsilon(|y_i^{k+1}|^2) - 2\Psi_\varepsilon(|y_i^k|^2) - \Psi'_\varepsilon(|y_i^k|^2)(|y_i^{k+1}|^2 - |y_i^k|^2) \leq 0.$$

Then, using (2.12)-(2.14), we get

$$(2.15) \quad J_\varepsilon(x^{k+1}) + \frac{1}{2}|A(x^{k+1} - x^k)|_2^2 + \sum_i \Psi'_\varepsilon(|y_i^k|^2)|y_i^{k+1} - y_i^k|^2 \leq J_\varepsilon(x^k).$$

From (2.15) and the coercivity of J_ε , it follows that $\{x^k\}_{k=1}^\infty$ and thus $\{y^k\}_{k=1}^\infty$ are bounded. Consequently, from (2.15) and (2.7), there exists a constant $\kappa > 0$ such that

$$(2.16) \quad J_\varepsilon(x^{k+1}) + \frac{1}{2}|A(x^{k+1} - x^k)|_2^2 + \kappa|y^{k+1} - y^k|_2^2 \leq J_\varepsilon(x^k).$$

Conditions (a) (ii), (b) (ii) respectively imply that $J_\varepsilon(x_k)$ is strictly decreasing unless $x^k = x^{k+1}$. In the latter case from (2.10) we infer that x^k solves (2.9), from which we conclude the first part of the theorem.

From (2.16), we conclude that

$$(2.17) \quad \sum_{k=0}^{\infty} |A(x^{k+1} - x^k)|_2^2 + \kappa|y^{k+1} - y^k|_2^2 < \infty.$$

Since $\{x^k\}_{k=1}^\infty$ is bounded, there exists a subsequence and $\bar{x} \in \mathbb{R}^n$ such that $x^{k_i} \rightarrow \bar{x}$. By (2.17) we get

$$\lim_{k \rightarrow \infty} |A(x^{k+1} - x^k)|_2^2 + \kappa|y^{k+1} - y^k|_2^2 = 0.$$

Then by using the coercivity of A under assumption (a) and the fact that $\text{Ker}(A) \cap \text{Ker}(\Lambda) = \{0\}$ under assumption (b), we conclude that

$$\lim_{k \rightarrow \infty} (x^{k+1} - x^k) = 0$$

and hence $x^{k_l+1} \rightarrow \bar{x}$. We can now pass to the limit with respect to k in (2.10), to obtain that \bar{x} is a solution to (2.9). \square

In the following proposition we establish the convergence of (2.5) to (2.1) as ε goes to zero.

Proposition 2.4. *Assume (H) and either (a) or (b). Denote by $\{x_\varepsilon\}_{\varepsilon>0}$ a solution to (2.5). Then any cluster point of $\{x_\varepsilon\}_{\varepsilon>0}$, of which there exists at least one, is a solution of (2.1).*

Proof. From the coercivity of J_ε we have that $\{x_\varepsilon\}_\varepsilon$ is bounded for ε small. Hence there exists a subsequence and $\bar{x} \in \mathbb{R}^n$ such that $x_{\varepsilon_l} \rightarrow \bar{x}$.

By property (H) (i) of ϕ , we have

$$(2.18) \quad \lim_{t \rightarrow 0} \phi(t) = 0 \quad \text{and} \quad \phi'(t) \geq 0 \quad \forall t \geq 0.$$

Moreover by the concavity of the function ϕ we have

$$\phi(t) - \phi(s) \leq \phi'(s)(t - s) \quad \text{for } s \in (0, \infty), t \in [0, \infty)$$

and by choosing $s = \varepsilon$ and $t = 0$ and by (2.18), we get for ε small enough

$$(2.19) \quad \phi'(\varepsilon)\varepsilon \rightarrow 0 \quad \text{as } \varepsilon \rightarrow 0.$$

By the definition of Ψ_ε , (2.18) and (2.19) we obtain that $\Psi_\varepsilon(t)$ converges uniformly to $\phi(\sqrt{t})$ as $\varepsilon \rightarrow 0$, equivalently

$$\sup_{t \in [0, \infty)} \left| \Psi_\varepsilon(t) - \phi(\sqrt{t}) \right| \rightarrow 0 \quad \text{as } \varepsilon \rightarrow 0,$$

from which we obtain

$$(2.20) \quad \Psi_\varepsilon(|\Lambda x_\varepsilon|^2) = \sum_{i=1}^r \Psi_\varepsilon(|(\Lambda x_\varepsilon)_i|^2) \rightarrow \sum_{i=1}^r \phi(\Lambda x_\varepsilon)_i = \Phi(\Lambda \bar{x}) \quad \text{as } \varepsilon \rightarrow 0.$$

Since $\{x_\varepsilon\}_\varepsilon$ solves (2.5), by letting $\varepsilon \rightarrow 0$ and using (2.20), we easily get that \bar{x} is a solution of (2.1). \square

2.4. Asymptotic behaviour as $\lambda \rightarrow 0^+$ and $\tau \rightarrow 0^+$ for the power law. We discuss the asymptotics as λ and τ go to zero in (2.1) for $\phi(t) = |t|^\tau, \tau \in (0, 1]$, which we repeat for convenience

$$(2.21) \quad \min_{x \in \mathbb{R}^n} \frac{1}{2} |Ax - b|_2^2 + \lambda |Ax|_\tau^\tau,$$

where A, b, Λ are as in (2.1), $\tau \in (0, 1], \lambda > 0$ and

$$|Ax|_\tau^\tau = \sum_{i=1}^r |(\Lambda x)_i|^\tau.$$

First we analyse the convergence as $\lambda \rightarrow 0$ for any fixed $\tau > 0$. We denote by P the orthogonal projection of \mathbb{R}^n onto $\text{Ker}(A^*)$ and set $\tilde{b} = (I - P)b \in \text{Rg}(A)$. Then

$$|Ax - b|_2^2 = |Ax - \tilde{b}|_2^2 + |Pb|_2^2.$$

For $\tau > 0$ fixed consider the problem

$$(2.22) \quad \min |Ax|_\tau^\tau \quad \text{subject to } Ax - \tilde{b} = 0,$$

Theorem 2.5. *Let $\text{rank}(A) = n$. For $\tau > 0$ fixed, let x_λ be a minimizer of (2.21) for any given $\lambda > 0$. Let $\tilde{x} \in \mathbb{R}^n$ be such that $A\tilde{x} = \tilde{b}$. Then every cluster point of solutions x_λ to (2.21) as $\lambda \rightarrow 0^+$ is a solution to (2.22).*

Proof. By optimality of x_λ we have

$$(2.23) \quad \frac{1}{2}|Ax_\lambda - \tilde{b}|_2^2 + \lambda|\Lambda x_\lambda|_\tau^\tau \leq \frac{1}{2}|A\tilde{x} - \tilde{b}|_2^2 + \lambda|\Lambda\tilde{x}|_\tau^\tau = \lambda|\Lambda\tilde{x}|_\tau^\tau,$$

from which we conclude that $\lim |Ax_\lambda - \tilde{b}|_2^2 = 0$ as $\lambda \rightarrow 0^+$.

Since $\text{rank}(A) = n$, the sequence $\{x_\lambda\}_{\lambda>0}$ is bounded in λ . Then there exists $\bar{x} \in \mathbb{R}^n$ and a subsequence $x_{\lambda_i} \rightarrow \bar{x}$ satisfying $A\bar{x} = \tilde{b}$. From (2.23) we have

$$|\Lambda x_\lambda|_\tau^\tau \leq |\Lambda\tilde{x}|_\tau^\tau \quad \text{for all } \tilde{x} \text{ satisfying } A\tilde{x} = \tilde{b}.$$

Taking the limit as $\lambda \rightarrow 0^+$, we conclude that \bar{x} is a solution to (2.22). \square

Now we prove the convergence as $\tau \rightarrow 0$ for any fixed $\lambda > 0$ of (2.21) to the related ℓ^0 -problem

$$(2.24) \quad \min_{x \in \mathbb{R}^n} \frac{1}{2}|Ax - b|_2^2 + \lambda|x|_0,$$

where for any $x \in \mathbb{R}^n$

$$|x|_0 = \sum_{k=1}^n |x_k|^0 = \text{number of nonzero elements of } x.$$

The precise statement is given in the following theorem.

Theorem 2.6. *Let $\text{rank}(A) = n$ and let $\lambda > 0$ be fixed. Then any cluster point (of which there exists at least one) of solutions $\{x_\tau\}$ to (2.21) converges as $\tau \rightarrow 0^+$ to a solution of (2.24).*

Proof. $\text{Rank}(A) = n$ ensures the existence of a converging subsequence (denoted with the same symbol) $\{x_\tau\} \rightarrow \bar{x}$ for some $\bar{x} \in \mathbb{R}^n$. For any fixed $i \in \{1, \dots, r\}$, denote $y_\tau = |(\Lambda x_\tau)_i|$ and $\bar{y} = |(\Lambda \bar{x})_i|$ and notice that $y_\tau \rightarrow \bar{y}$ as $\tau \rightarrow 0$. Then if $\bar{y} = 0$, we can assume $y_\tau < 1$ for τ enough small and we conclude

$$y_\tau^\tau < y_\tau \rightarrow 0 \quad \text{as } \tau \rightarrow 0.$$

If $\bar{y} > 0$ we have

$$\log(y_\tau^\tau) = \tau \log(y_\tau) \rightarrow 0 \quad \text{as } \tau \rightarrow 0$$

and thus

$$y_\tau^\tau \rightarrow 1 \quad \text{as } \tau \rightarrow 0.$$

By using the above arguments for all $i = 1, \dots, r$, we have

$$|(\Lambda x_\tau)_i|^\tau \rightarrow |(\Lambda \bar{x})_i|^0 \quad \text{as } \tau \rightarrow 0$$

and then we conclude

$$(2.25) \quad |\Lambda x_\tau|_\tau^\tau \rightarrow |\Lambda \bar{x}|_0 \quad \text{as } \tau \rightarrow 0.$$

By the optimality of x_τ we have

$$\frac{1}{2}|Ax_\tau - b|_2^2 + \lambda|\Lambda x_\tau|_\tau^\tau \leq \frac{1}{2}|Ax - b|_2^2 + \lambda|\Lambda x|_\tau^\tau, \quad \text{for all } x \in \mathbb{R}^n.$$

Then the proof follows by taking the limit $\tau \rightarrow 0$ and using (2.25) to obtain

$$\frac{1}{2}|A\bar{x} - b|_2^2 + \lambda|\Lambda \bar{x}|_0 \leq \frac{1}{2}|Ax - b|_2^2 + \lambda|\Lambda x|_0, \quad \text{for all } x \in \mathbb{R}^n.$$

\square

3. ALGORITHM AND NUMERICAL RESULTS

For convenience we recall the algorithm in the following form.

Algorithm 1 Monotone algorithm with ε -continuation strategy

- 1: Initialize x^0 , ε^0 , and set $y^0 = \Lambda x^0$. Set $k = 0$;
- 2: **repeat**
- 3: Solve for x^{k+1}

$$A^*Ax^{k+1} + \Lambda^* \frac{1}{\max\left\{\frac{\varepsilon}{\phi'(\varepsilon)}, \frac{|y^k|}{\phi'(|y^k|)}\right\}} \Lambda x^{k+1} = A^*b.$$

- 4: Set $y^{k+1} = \Lambda x^{k+1}$.
 - 5: Set $k = k + 1$.
 - 6: **until** the stopping criterion is fulfilled.
 - 7: Reduce ε and repeat 2.
-

Remark 3.1. Note that an ε -continuation strategy is performed, that is, the procedure is performed for an initial value ε^0 and then ε is decreased up to a certain value. More specifically, in all our experiments, ε is initialized with 10^{-1} and decreased up to 10^{-12} .

Remark 3.2. The stopping criterion is based on the l^∞ -norm of the equation (2.9) and the tolerance is set to 10^{-3} in all the following examples, except for the fracture problem where it is of the order of 10^{-15} .

In the following subsection we present our numerical results in cohesive fracture mechanics. Then in subsection 3.2 the performance of our algorithm is compared to two other schemes for nonconvex and nonsmooth optimization problems.

3.1. Application to quasi-static evolution of cohesive fracture models. In this section we focus on the numerical realization of quasi-static evolutions of cohesive fractures. This kind of problems require the minimization of an energy functional, which has two components: the elastic energy and the cohesive fracture energy. The underlying idea is that the fracture energy is released gradually with the growth of the crack opening. The cohesive energy, denoted by θ , is assumed to be a monotonic non-decreasing function of the jump amplitude of the displacement, denoted by $\llbracket u \rrbracket$. Cohesive energies were introduced independently by Dugdale [13] and Barenblatt [4], we refer to [34] for more details on the models. Let us just remark that the two models differ mainly in the evolution of the derivative $\theta'(\llbracket u \rrbracket)$, that is, the *bridging force*, across a crack amplitude $\llbracket u \rrbracket$. In Dugdale's model this force keeps a constant value up to a critical value of the crack opening and then drops to zero. In Barenblatt's model, the dependence of the force on $\llbracket u \rrbracket$ is continuous and decreasing.

In this section we test the ℓ^τ -term $0 < \tau < 1$ as a model for the cohesive energy. In particular, the cohesive energy is not differentiable in zero and the bridging force goes to infinity when the jump amplitude goes to zero. Note also that the bridging force goes to zero when the jump amplitude goes to infinity.

we denote by $u : \Omega \rightarrow \mathbb{R}$ the displacement function. The deformation of the domain is given by an external force which we express in terms of an external displacement function $g : \Omega \times [0, T] \rightarrow \mathbb{R}$. We require that the displacement u coincides with the external deformation, that is

$$u|_{\partial\Omega} = g|_{\partial\Omega}.$$

We denote by Γ the point of the (potential) crack, and by $\theta(\llbracket u \rrbracket)_\Gamma$ the value of the cohesive energy θ on the crack amplitude of the displacement $\llbracket u \rrbracket$ on Γ . Since we are in a quasi-static setting, we introduce the time discretization $0 = t_0 < t_1 < \dots < t_T = T$ and look for the equilibrium configurations which are minimizers of the energy of the system. This means that for each $i \in \{0, \dots, T\}$ we need to minimize the energy of the system

$$J(u) = \frac{1}{2} \int_{\Omega \setminus \Gamma} |a(x) \nabla u|^2 dx + \theta(\llbracket u \rrbracket)_\Gamma$$

with respect to a given boundary datum g :

$$u^* \in \operatorname{argmin}_{u=g(t_i) \text{ on } \partial\Omega} J(u).$$

The function $a(\cdot)$ measures the degree of homogeneity of the material, e.g. $a(x) \equiv 1$ means that the material is homogeneous.

In our experiments, we consider three different types of cohesive energy, the ℓ^τ $\tau \in (0, 1)$, SCAD and MCP penalties as defined in (2.2), (2.3), (2.4) respectively.

In paragraphs 3.1.1 and 3.1.2 we show our results for one-dimensional and two-dimensional experiments, respectively.

3.1.1. One-dimensional experiments. We consider the one-dimensional domain $\Omega = [0, 1]$ and we chose the point of crack as the midpoint $\Gamma = 0.5$. We divide Ω into $2N$ intervals and approximate the displacement function with a function u_h that is piecewise linear on $\Omega \setminus \Gamma$ and has two degrees of freedom on Γ to represent correctly the two lips of the fracture, denoting with u_N^- the one on $[0, 0.5]$ and u_N^+ the one on $[0.5, 1]$. We discretize the problem in the following way

$$(3.1) \quad J_h(u_h) = \frac{1}{2} \sum_{i=1}^{2N} 2N |a_i (u_i - u_{i-1})|^2 + \theta(\llbracket u_N \rrbracket),$$

where if $i \leq N$ we identify $u_N = u_N^-$ while for $i > N$, $u_N = u_N^+$ and a_h denotes the piecewise linear approximation of the material inhomogeneity function. We remark that the jump of the displacement is not taken into account in the sum, and the gradient of u is approximated with finite difference of first order. The Dirichlet condition is applied on $\partial\Omega = \{0, 2l\}$ and the external displacement is chosen as

$$u(0, t) = 0, \quad u(2l, t) = 2lt.$$

To enforce the boundary condition in the minimization process, we add it to the energy functional as a penalization term. Hence, we solve the following unconstrained minimization problem

$$(3.2) \quad \min N |Au_h - b|_2^2 + \theta(\llbracket u_N \rrbracket),$$

where the operator $A \in \mathbb{R}^{(2N+1) \times (2N+1)}$ is given by $A = RD$ where $R \in \mathbb{R}^{(2N+1) \times (2N+1)}$ is the diagonal operator with i -entries $R_{ii} = a_i$ and

$$A = \begin{bmatrix} \bar{D} & & & & \\ 0 & \dots & 0 & \gamma & \end{bmatrix}.$$

Here $\bar{D} \in \mathbb{R}^{2N \times (2N+1)}$ denotes the backward finite difference operator $D : \mathbb{R}^{2N+1} \rightarrow \mathbb{R}^{2N+1}$ without the $N+1$ row, where D is defined as

$$(3.3) \quad D = \begin{pmatrix} 1 & 0 & 0 & \dots & 0 \\ -1 & 1 & 0 & \dots & 0 \\ \vdots & \vdots & \vdots & \ddots & \vdots \\ 0 & \dots & 0 & -1 & 1 \end{pmatrix}.$$

Moreover $b \in \mathbb{R}^{2N+1}$ in (3.2) is given by $b = (0, \dots, \gamma t_i)'$ and γ is the penalization parameter. To compute the jump between the two lips of the fracture, we introduce the operator $D_f : \mathbb{R}^{2N+1} \rightarrow \mathbb{R}$ defined as $D_f = (0, \dots, -1, 1, 0, \dots, 0)$ where -1 and 1 are respectively in the N and $N + 1$ positions. Then we write the functional (3.2) as follows

$$(3.4) \quad \min N |Au_h - b|_2^2 + \theta(D_f u),$$

We consider the three different penalizations given by the $\ell^\tau, \tau \in (0, 1)$, the SCAD and the MCP penalties. Note that $\text{Ker} A = 0$, hence assumptions (a)(ii) and (c)(ii) are satisfied and existence of a minimizer for (3.4) is guaranteed.

Our numerical experiments were conducted with a discretization in $2N$ intervals with $N = 100$. The time step in the time discretization of $[0, T]$ with $T = 3$ is set to $dt = 0.01$. The parameters of the energy functional $J_h(u_h)$ are set to $\lambda = 1, \gamma = 50$.

We remark that in the following experiments the material function $a(x)$ was always chosen as the identity. For tests with more general $a(x)$, we refer to the two-dimensional experiments reported in the following subsection. In Figures 1, 2 we report our results obtained by **Algorithm 1** respectively for the models ℓ^p and SCAD. In each figure we show time frames to represent the evolutions of the crack for different values of the parameter τ . Each time frame consists of three different time steps (t_1, t_2, t_3) , where t_2, t_3 are chosen as the first instant where the prefraction and the fracture appear.

We observe the three phases that we expect from a cohesive fracture model:

- *Pure elastic deformation*: in this case the jump amplitude is zero and the gradient of the displacement is constant in $\Omega \setminus \Gamma$;
- *Prefracture*: the two lips of the fracture do not touch each other, but they are not free to move. The elastic energy is still present.
- *Fracture*: the two parts are free to move. In this final phase the gradient of the displacement (and then the elastic energy) is zero.

We remark that the formation of the crack is anticipated for smaller values of τ . As we see in Figure 1, for $\tau = .01$ prefraction and fracture are reached at $t = .3$ and $t = 1.5$ respectively. As τ is increased to $\tau = .1$, prefraction and fracture occur at $t = 1$ and $t = 3$ respectively. We observe the same phenomenon for the SCAD (see Figure 2).

We tested our algorithm also for the MCP model, where no prefraction phase can be observed, that is, the displacement breaks almost instantaneously to reach the complete fracture.

Finally we remark that in our experiments the residue is $O(10^{-16})$ and the number of iterations is small, e.g. 12, 15 for $\tau = .01, .1$ respectively.

3.1.2. Two-dimensional experiments. We consider the two-dimensional domain $\Omega = (0, 1) \times (0, 1)$ and we chose the one-dimensional subdomain $0.5 \times (0, 1)$ as the line of crack. We proceed in the discretization of the problem analogously as in subsection 3.1.1, that is, we divide $[0, 1]$ into $2N$ intervals and approximate the displacement function with a function u_h that is piecewise linear in $\Omega \setminus \Gamma$ and has two degrees of freedom on Γ to represent correctly the two lips of the fracture. Define the operator $A \in \mathbb{R}^{(2N+1) \times (2N+1)}$ by

$$A = \begin{bmatrix} R^1 D_1 \\ R^2 D_2 \\ \gamma I_{m^2} \end{bmatrix},$$

where $m = 2N + 2$, $R^1, R^2 \in \mathbb{R}^{(2N+1) \times (2N+1)}$ are two diagonal operators approximating the degree of homogeneity of the material, $D_1 \in \mathbb{R}^{(m-1)(m-2) \times m^2}$, $D_2 \in \mathbb{R}^{m(m-2) \times m^2}$ are defined as $D_1 = G_1((m-1)N + 1 : (m-1)N + 2(m-1), :) = [\quad]$, $D_2 = G_2(mN + 1 : mN + m, :) = [\quad]$,

where $G_1, G_2 \in \mathbb{R}^{m(m-1) \times m^2}$ are defined as follows

$$G_1 = \text{kron}(I_m, D), \quad G_2 = \text{kron}(D, I_m)$$

and $D \in \mathbb{R}^{m-1 \times m}$ denotes the following backward finite difference operator

$$(3.5) \quad D = \begin{pmatrix} -1 & 1 & 0 & \cdots & \cdots & 0 \\ 0 & -1 & 1 & 0 & \cdots & 0 \\ \vdots & \vdots & \vdots & \vdots & \vdots & \vdots \\ 0 & \cdots & \cdots & 0 & -1 & 1 \end{pmatrix}.$$

Again we enforce the boundary condition by adding it to the energy functional as a penalization term. Hence, we solve the following unconstrained minimization problem

$$(3.6) \quad \min |Au_h - b|_2^2 + \theta(D_f u),$$

where $b \in \mathbb{R}^{(m-2)(2m-1)+m^2}$ in 3.6 is given by $b = (0, \dots, \gamma g(t_i))'$, $g(t_i)$ is the discretization of the boundary datum g at time t_i and γ is the penalization parameter. Moreover the jump of the crack is represented by the operator $D_f \in \mathbb{R}^{m \times m^2}$ defined as follows

$$D_f = [0_{m,mN}, -I_m, I_m, 0_{m,m^2-mN-2m}]$$

where by $0_{r,s}$ we denote the null matrix of dimension $r \times s$.

Our numerical experiments were conducted with a discretization in $2N$ intervals with $N = 80$. The time step in the time discretization of $[0, T]$ with $T = 3$ is set to $dt = 0.01$. The parameters of the energy functional $J_h(u_h)$ are set to $\lambda = 1, \gamma = 50$. We perform two different series of experiments with boundary data respectively resulting from evaluating g_1, g_2 on $\partial\Omega$, where

$$g_1(t)(x) = (2x_1 - 0.5)t \quad \text{for every } t \in [0, 1], x = (x_1, x_2) \in \Omega$$

and the other one with boundary datum

$$g_2(t)(x) = 2t \cos(4(x_2 - 0.5))(x_1 - 0.5) \quad \text{for every } t \in [0, 1], x = (x_1, x_2) \in \Omega.$$

In Figures 3, 4, 5, 6 we show the results obtained with boundary datum g_1 for each of the considered models, that is, ℓ^τ , SCAD and MCP and in Figures 7 the ones with boundary datum g_2 for the ℓ^τ model. In the case of boundary datum g_2 we tested our algorithm also on the SCAD and the MCP models, obtaining similar results to the ones shown in Figure 7. In these first experiments, the diagonal operators R_1, R_2 are taken as the identity, that is, we suppose to have an homogeneous material.

As expected from a cohesive fracture model, we observe the three phases of pure elastic deformation, prefracture and fracture.

Also, prefracture and fracture are reached at different times for different values of τ , typically they are anticipated for smaller values of τ .

When the boundary datum is g_2 , that is, not constant in the y direction, we note that the fracture is reached before in the part of the fracture line corresponding to the part of the boundary where the datum is bigger.

In Figures 8, 9, 10 we tested the algorithm in case of a non homogeneous material. In Figure 8 we show the result for a two-material specimen, that is, we took

$$(3.7) \quad \begin{cases} R_{ii}^1 = 600 & i = 1, \dots, (m-1)(N+1), \\ R_{ii}^1 = 1 & i = (m-1)(N+1) + 1, \dots, 2(m-1)(N+1) \end{cases}$$

$$(3.8) \quad \begin{cases} R_{ii}^2 = 600 & i = 1, \dots, mN, \\ R_{ii}^2 = 1 & i = mN + 1, \dots, 2mN \end{cases}$$

Note that, for the above values of R^1, R^2 , the slides of the specimen show an asymmetric behaviour, namely the displacement is flatter where the material function is bigger (that is, when $R_{ii}(x) = 600$).

In Figure 9,10 we report the results when R^1, R^2 are the discretization of the following function

$$(3.9) \quad \begin{cases} r(x, y) = 400 \exp(y), & \text{for } x \leq N \\ r(x, y) = 400y & \text{otherwise} \end{cases}$$

Note that in Figure 10 the boundary datum is chosen as

$$g_3(t) = \frac{1}{100} \cos(2(y - 0.5))(x - 0.5).$$

As expected due to the choice of R^1, R^2 , we remark an asymmetric behaviour of the fracture in the y direction, namely the specimen brakes before where the material function is higher.

3.2. Comparison with GIST. In this section we present the result of experiments to compare the performance of **Algorithm 1** with the following two other algorithms for nonconvex and nonsmooth minimization. We first compare with the GIST "General Iterative Shrinkage and Thresholding" algorithm for ℓ^τ , $\tau < 1$ minimization. We took advantage of the fact that for GIST¹ an open source toolbox is available, which facilitated an unbiased comparison. Moreover, in [33] several tests were made to compare GIST and IRLS "Iteratively reweighted least squares", showing that the two algorithms have nearly the same performance, with only significant difference in speed, where GIST appears to be the faster one.

Concerning ℓ^1 -minimization based algorithms, we compared our algorithm with the FISTA "Fast Iterative Shrinkage-Thresholding Algorithm", see subsection 3.2.

We remark that the results of [33] show no particular differences in the performance of the algorithm for different values of τ , except that the speed becomes much worse for τ near to 1, say $\tau = 0.9$. Motivated also by this observations, the comparisons explained in the following were made for one fixed value of τ .

The comparison is carried out through the following three examples, the academical M-matrix problem, an optimal control problem and a microscopy imaging reconstruction example.

The monotone algorithm is stopped when the ℓ^∞ -residue of the optimality condition 2.9 is of the order of 10^{-3} in the M-matrix and optimal control problems and of the order of 10^{-8} in the imaging example. GIST is terminated if the relative change of the two consecutive objective function values is less than 10^{-5} or the number of iterations exceeds 1000. We remark that no significant changes were remarked by setting a lower tolerance than 10^{-5} or a bigger number of maximal iteration for GIST.

Since both GIST and the FISTA solve the problem (2.1) when the operator Λ coincides with the identity, we also make this choice in the following subsections. Finally we remark that the three examples were analysed already in [20] with different aims.

3.2.1. M-matrix example. We consider

$$(3.10) \quad \min_{x \in \mathbb{R}^{n \times n}} J(x) = \min_{x \in \mathbb{R}^{n \times n}} \frac{1}{2} \|Ax - b\|_2^2 + \lambda |x|_\tau^\tau,$$

A is the forward finite difference gradient

$$A = \begin{pmatrix} G_1 \\ G_2 \end{pmatrix},$$

¹The reference paper is [38], the toolbox can be found in <https://github.com/rflamary/nonconvex-optimization>.

with $G_1 \in \mathbb{R}^{n(n+1) \times n^2}$, $G_2 \in \mathbb{R}^{n(n+1) \times n^2}$ as

$$G_1 = I \otimes D, \quad G_2 = D \otimes I,$$

I is the $n \times n$ identity matrix, \otimes the tensor product, $D = (n+1)\tilde{D}$, $\tilde{D} \in \mathbb{R}^{(n+1) \times n}$ is

$$\begin{pmatrix} 1 & 0 & 0 & \cdots & 0 \\ -1 & 1 & 0 & \cdots & 0 \\ & & & & \\ 0 & \cdots & 0 & -1 & 1 \\ 0 & \cdots & 0 & 0 & -1 \end{pmatrix}.$$

Then $A^T A$ is an M matrix coinciding with the 5-point star discretization on a uniform mesh on a square of the Laplacian with Dirichlet boundary conditions. Moreover (3.10) can be equivalently expressed as

$$(3.11) \quad \min_{x \in \mathbb{R}^{n \times n}} \frac{1}{2} |Ax|_2^2 - (x, f) + \lambda |x|_\tau^\tau,$$

where $f = A^T b$. If $\lambda = 0$ this is the discretized variational form of the elliptic equation

$$(3.12) \quad -\Delta y = f \text{ in } \Omega, \quad y = 0 \text{ on } \partial\Omega.$$

For $\lambda > 0$ the variational problem (3.11) gives a sparsity enhancing solution for the elliptic equation (3.12), that is, the displacement y will be 0 when the forcing f is small. Our tests are conducted with f chosen as discretization of $f = 10x_1 \sin(5x_2) \cos(7x_1)$. The initialization is chosen as the solution of the corresponding non-sparse optimization problem.

We remark that in [19] and [20] the algorithm was also tested in the same situation for different values of τ and λ , showing, in particular and consistent with our expectations, that the sparsity of the solution increases with λ .

Here we focus on the comparison between the performances of **Algorithm 1** and GIST. In order to compare the two schemes, we focus on the value of the unregularized functional J in (3.10) reached by both algorithms, the time to acquire it, and the number of iterations. Our tests were conducted for $\tau = 0.5$, and λ incrementally increasing from 10^{-3} to 0.3, see the following tables. The parameter ε was decreased from 10^{-1} to 10^{-6} . These values are reported in Table 1, 2 and 3, 4 for GIST and **Algorithm 1** respectively.

We observe that **Algorithm 1** achieves always lower values of the functional J , but in a longer time. The number of iterations needed by **Algorithm 1** is smaller than the number of iterations of GIST for small values of λ , more precisely for $\lambda < 0.1$. Note that for smaller λ the number of iterations of **Algorithm 1** is smaller than the one of GIST. This suggests, consistent with our expectation, that the monotone scheme is slower than GIST mainly because it solves a nonlinear equation at each iteration.

We carried out a further test in order to measure the timing performance of **Algorithm 1**, that is, the algorithm is stopped as soon as the value of J achieved by GIST is reached. In Table 4, 5 we report the time, the number of iterations, the values of J , and the value of ε reached. We observe that the time is almost always smaller than the one of GIST, except for values of λ bigger or equal than $\lambda = 0.15$. Also, for these values, the differences in the time are very small.

3.2.2. *Optimal control problem.* We consider the linear control system

$$\frac{d}{dt} y(t) = Ay(t) + Bu(t), \quad y(0) = 0,$$

λ	0.01	0.05	0.10	0.15	0.2	0.3
J	246.324	264.232	285.26	303.685	319.737	338.998
time	0.563	0.701	0.444	0.468	0.461	0.61
iterations	293	384	249	247	216	209

TABLE 1. M-matrix example. Value of J, time, iterations of GIST.

λ	0.01	0.05	0.10	0.15	0.2	0.3
J	246.186	263.92	284.079	301.327	315.553	331.71
time	10.92	26.142	56.397	33.021	124.624	31.423
iterations	149	361	779	456	1722	433

TABLE 2. M-matrix example. Value of J, time, iterations of **Algorithm 1**.

λ	0.001	0.01	0.05	0.1	0.15	0.2
J_{GIST}	242.158	246.324	264.232	285.26	303.685	319.737
iter_{mon}	1	1	5	5	6	7
time_{mon}	0.085	0.082	0.39	0.387	0.478	0.673
$\text{time}_{\text{GIST}}$	0.445	0.563	0.701	0.444	0.468	0.461

TABLE 3. M-matrix example. Value of the functional, iterations, time to which **Algorithm 1** overcome GIST's.

that is,

$$(3.13) \quad y(T) = \int_0^T e^{\mathcal{A}(T-s)} B u(s) ds,$$

where the linear closed operator \mathcal{A} generates a C_0 -semigroup $e^{\mathcal{A}t}$, $t \geq 0$ on the Hilbert space X . More specifically, we consider the one-dimensional controlled heat equation for $y = y(t, x)$:

$$(3.14) \quad y_t = y_{xx} + b_1(x)u_1(t) + b_2(x)u_2(t), \quad x \in (0, 1),$$

with homogeneous boundary conditions $y(t, 0) = y(t, 1) = 0$ and thus $X = L^2(0, 1)$. The differential operator $\mathcal{A}y = y_{xx}$ is discretized in space by the second order finite difference approximation with $n = 49$ interior spatial nodes ($\Delta x = \frac{1}{50}$). We use two time dependent controls $\vec{u} = (u_1, u_2)$ with corresponding spatial control distributions b_i chosen as step functions:

$$b_1(x) = \chi_{(.2, .3)}, \quad b_2(x) = \chi_{(.6, .7)}.$$

The control problem consists in finding the control function \vec{u} that steers the state $y(0) = 0$ to a neighbourhood of the desired state y_d at the terminal time $T = 1$. We discretize the problem in time by the mid-point rule, i.e.

$$(3.15) \quad A \vec{u} = \sum_{k=1}^m e^{\mathcal{A}(T-t_k - \frac{\Delta t}{2})} (B \vec{u})_k \Delta t,$$

where $\vec{u} = (u_1^1, \dots, u_1^m, u_2^1, \dots, u_2^m)$ is a discretized control vector whose coordinates represent the values at the mid-point of the intervals (t_k, t_{k+1}) . Note that in (3.15) we denote by B

a suitable rearrangement of the matrix B in (3.13) with some abuse of notation. A uniform step-size $\Delta t = \frac{1}{50}$ ($m = 50$) is utilized. The solution of the control problem is based on the sparsity formulation (2.1), where $\Lambda = I$ and $\phi_{\lambda,\tau}(x) = \lambda|x|^\tau$ and b in (2.1) is the discretized target function chosen as the Gaussian distribution $y_d(x) = 0.4 \exp(-70(x - .7)^2)$ centered at $x = .7$. That is, we apply our algorithm for the discretized optimal control problem in time and space where x from (2.1) is the discretized control vector $u \in \mathbb{R}^{2m}$ which is mapped by A to the discretized output y at time 1 by means of (3.15). Moreover b from (2.1) is the discretized state y_d with respect to the spatial grid Δx . The parameter ε was initialized with 10^{-3} and decreased down to 10^{-8} .

Similarly as in the previous subsection, we compare the values of the functional, the time and the number of iterations. The experiments are carried out for $\tau = 0.5$ and λ in the interval 10^{-3} -0.2. We report only the values for the second control u_2 since the first control u_1 is always zero (as expected).

As can be seen from the following tables, the same kind of remarks as in the previous subsection apply. In particular GIST is faster but less precise than **Algorithm 1**, but **Algorithm 1** overcomes the value reached by GIST more rapidly.

λ	0.0001	0.001	0.01	0.2
J	0.044	0.073	0.599	0.599
time	0.296	0.047	0.04	0.037
iterations	222	157	3	3

TABLE 4. Optimal control problem. Value of J, time, iterations of GIST.

λ	0.0001	0.001	0.01	0.2
J	0.042	0.068	0.185	0.599
time	11.758	15.140	14.866	12.501
iterations	35	28	32	27

TABLE 5. Optimal control problem. Value of J, time, iterations of **Algorithm 1**.

λ	0.0001	0.001	0.01	0.2
J_{mon}	0.043	0.071	0.185	0.599
iter_{mon}	1	1	5	5
time_{mon}	2.2	0.1	0.39	0.025
$\text{time}_{\text{GIST}}$	0.296	0.047	0.04	0.037

TABLE 6. Optimal control problem. Value of J, iterations, time for which **Algorithm 1** overcomes GIST's.

3.2.3. *Compressed sensing approach for microscopy image reconstruction.* We compare **Algorithm 1** and GIST in a microscopy imaging problem, in particular we focus on the STORM (stochastic optical reconstruction microscopy) method, based on stochastically switching and high-precision detection of single molecules to achieve an image resolution beyond the diffraction limit. The literature on the STORM has been intensively increasing, see e.g. [36], [5] [23], [26]. We refer in particular to [20] for a detailed description of the method and for more references.

Our approach is based on the following constrained-minimization problem:

$$(3.16) \quad \min_{x \in \mathbb{R}^n} |x|_\tau^\tau \quad \text{such that} \quad |Ax - b|_2 \leq \varepsilon,$$

where $\tau \in (0, 1]$, x is the up-sampled, reconstructed image, b is the experimentally observed image, and A is the impulse response (of size $m \times n$, where m and n are the numbers of pixels in b and x , respectively). A is usually called the point spread function (PSF) and describes the response of an imaging system to a point source or point object. Problem (3.16) can be reformulated as:

$$(3.17) \quad \min_{x \in \mathbb{R}^n} \frac{1}{2} |Ax - b|_2^2 + \lambda |x|_\tau^\tau.$$

First we tested the procedure for same resolution images, in particular the conventional and the true images are both 128×128 pixel images. Then the algorithm was tested in the case of a 16×16 pixel conventional image and a 128×128 true image. The values for the impulse response A and the measured data b were chosen according to the literature, in particular A was taken as the Gaussian PSF matrix with variance $\sigma = 8$ and size $3 \times \sigma = 24$, and b was simulated by convolving the impulse response A with a random 0-1 mask over the image adding a white random noise so that the signal to noise ratio is .01.

We carried out several tests with the same data for different values of τ, λ . We report only our results for $\tau = .1$ and $\lambda = 10^{-6}, \lambda = 10^{-9}$ for the same and the different resolution case respectively, since for these values the best reconstructions were achieved. We focus on two different type of images, a sparse 0-1 cross-like image and the standard phantom image. In order to compare the performance of **Algorithm 1** and the GIST algorithm, we focus on the number of surplus emitters (Error+) and missed emitters (Error-) recovered in the case of the cross image and different resolution. The errors are computed on an average over six recoveries for different values of the noise. The graphics of the errors against the noise are reported in Figures 11 and 12 for **Algorithm 1** and GIST respectively. We remark that these quantities are typically used as a measure of the efficacy of the reconstruction method, see for example [14] (where, under certain conditions, a linear decay with respect to the noise is proven) and [9].

The results shows that by GIST the Error- is always 197, whereas by **Algorithm 1** is always under 53 and even smaller for small values of the noise. On the other hand, the Error+ by GIST is always 0 and by **Algorithm 1** is zero for small values of the noise and then monotonically increasing until it reaches 175 when the noise is equal to 0.1. Consistently with what expected, by **Algorithm 1** the graphics show a linear decay w.r.t. the noise, differently from the behaviour showed by GIST. Moreover, the results found by **Algorithm 1** lead to more accuracy in the recovery, in the sense that the quantity of missed emitters is smaller, whereas on the other hand GIST seems to lead to a more sparser solutions (since the Error+ is 0 by GIST).

Finally we remark that in the case of the cross image GIST is faster than our algorithm, consistently with the result presented in the previous subsection and as expected, since our algorithm solves a nonlinear equation for each minimization problem. On the other hand, in the case of the standard phantom image GIST results to be far slower than **Algorithm 1**.

In Figure 13 we report the results obtained in the same situation by the FISTA "Fast Iterative Shrinkage Thresholding Algorithm" for ℓ^1 minimization. We remark that by the FISTA the

Error+ is always above 400, whereas by **Algorithm 1** is zero for small value of the noise. This shows that **Algorithm 1** leads to more sparsity with respect to the FISTA, consistently with our expectation since the FISTA is based on ℓ^1 minimization.

4. CONCLUSIONS

We have developed a monotone convergent algorithm for a class of nonconvex nonsmooth optimization problems arising in the modelling of fracture mechanics and in imaging reconstruction, including the ℓ^τ , $\tau \in (0, 1]$, the smoothly clipped absolute deviation and the minimax concave penalty. Theoretically, we established the existence of a minimizer of the original problem under assumptions implying coercivity of the functional. Then we derived necessary optimality conditions for a regularized version of the original problem. The optimality conditions for the regularized problem were solved through a monotonically convergent scheme based on an iterative procedure. We proved the convergence of the iteration procedure under the same assumptions that guarantee existence. A remarkable result is the strict monotonicity of the functional along the sequence of iterates generated by the scheme. Moreover we proved the convergence of the regularized problem to the original one as the regularization parameter goes to zero.

The procedure is very efficient and accurate. The efficiency and accuracy of the procedure was verified by numerical tests simulating the evolution of cohesive fractures and microscopy imaging. An issue of high relevance to us was the comparison of the scheme to two alternative algorithms, the GIST "General Iterative Shrinkage and Thresholding" algorithm for ℓ^τ minimization, with τ strictly positive and less than 1 and the FISTA "Fast Iterative Shrinkage-Thresholding Algorithm" for ℓ^1 minimization. We first compared with GIST by focusing on the infimal value reached by the iteration procedure and on the computing time. Our results showed that the monotone algorithm is able to reach a smaller value of the objective functional when compared to GIST's, therefore leading to a better accuracy. Finally we compared our scheme with FISTA in sparse recovery related to microscopy imaging. The results showed that the monotone scheme lead to more sparsity with respect to FISTA, as expected since FISTA concerns ℓ^1 minimization.

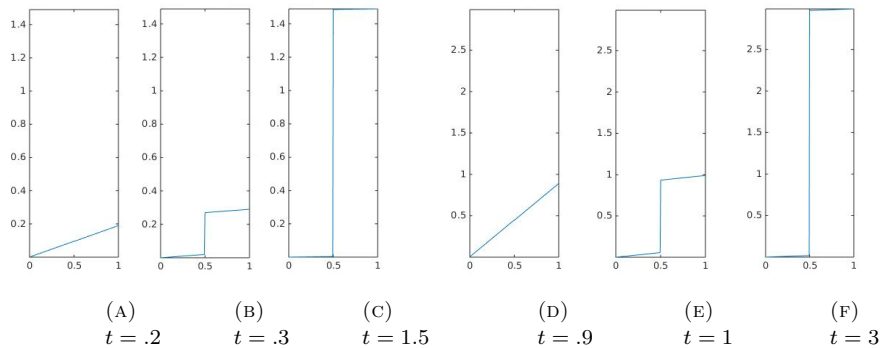


FIGURE 1. Three time-step evolution of the displacement for $\tau = .01$, $t = .2, .3, 1.5$ (left), $\tau = .1$, $t = .9, 1, 3$ (right). Results obtained by **Algorithm 1**.

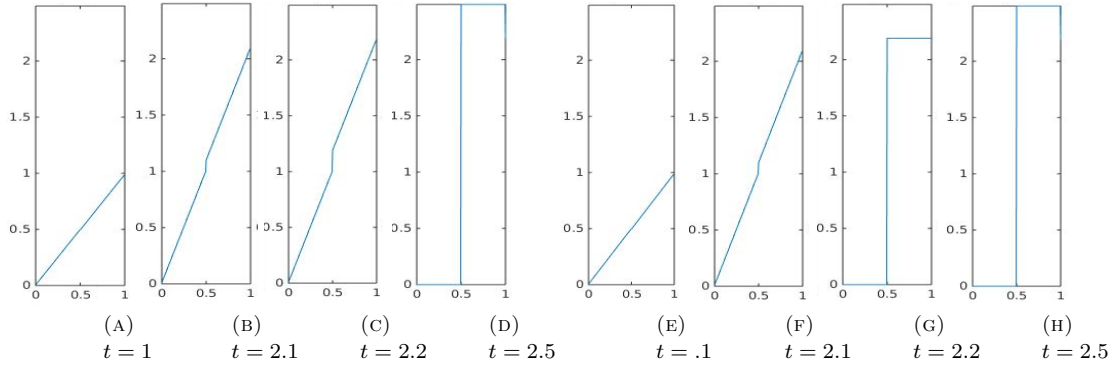


FIGURE 2. Four time-step evolution of the displacement for the SCAD model, $\tau = 20$, $t = 1, 2.1, 2.2, 2.5$ (left), $\tau = 10$, $t = .1, 2.1, 2.2, 2.5$ (right). Results obtained by **Algorithm 1**.

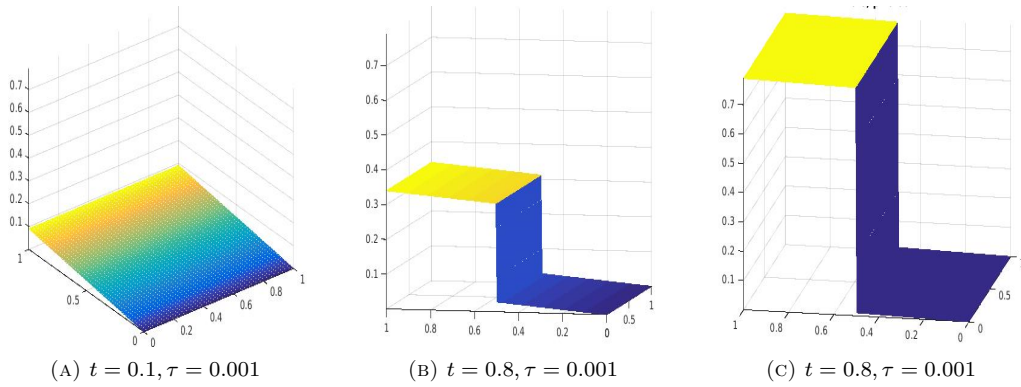


FIGURE 3. Displacement, $\theta(\cdot) = |\cdot|_{\tau}$, with $\tau = 0.001$, $R^1 = R^2 = I$, and boundary datum $g = g_1$

REFERENCES

- [1] M. Artina, M. Fornasier, F. Solombrino, *Linearly constrained nonsmooth and nonconvex minimization*, SIAM J. Optim., 23, 1904-1937 (2013).
- [2] M. Artina, F. Cagnetti, M. Fornasier, F. Solombrino, *Linearly constrained evolution of critical points and an application to cohesive fractures*, Math. Models Methods Appl. Sci., 27(02):231-290,2017.
- [3] H. P. Babcock, J. R. Moffitt, Y. Cao, X. Zhuang, *Fast compressed sensing analysis for super-resolution imaging using L1-homotopy*, Optics Express, 21 (2013), pp. 28583-28596.
- [4] G. I. Barenblatt, *The mathematical theory of equilibrium cracks in brittle fracture*, Adv. Appl. Math. Mech. 7 (1962), pp. 55-129.

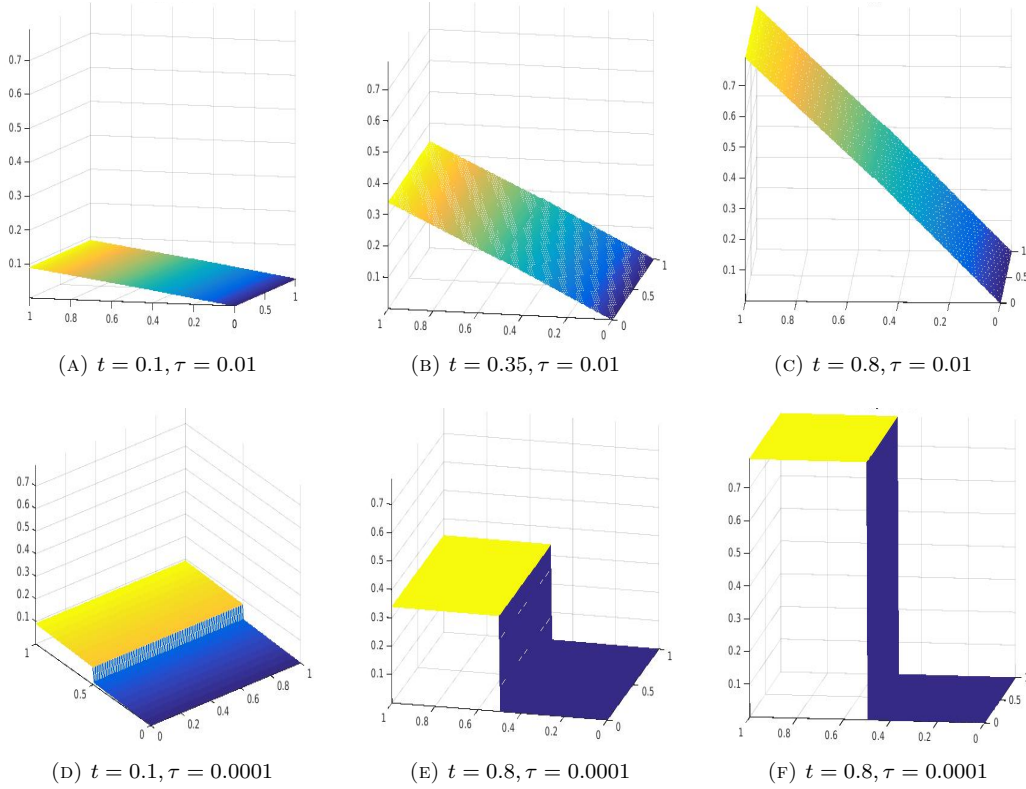


FIGURE 4. Displacement, $\theta(\cdot) = |\cdot| \frac{\tau}{\tau}$, comparison between $\tau = 0.01$ and $\tau = 0.0001$, $R^1 = R^2 = I$, boundary datum $g = g_1$.

- [5] E. Betzig, G. H. Patterson, R. Sougrat, O. W. Lindwasser, S. Olenych, J. S. Bonifacino, M. W. Davidson, J. Lippincott-Schwartz, H. F. Hess, *Imaging intracellular fluorescent proteins at nanometer resolution*, Science, 313 (2006), pp. 1642-1645.
- [6] K. Bredies, D.A. Lorentz, S. Reiterer, *Minimization of non-smooth, nonconvex functionals by iterative thresholding*, J. Optim. Theory Appl., 165 (2015), pp. 78-112.
- [7] P. Breheny, J. Huang. *Coordinate descent algorithms for nonconvex penalized regression, with applications to biological feature selection*, The annals of applied statistics, Vol.5, No. 1, 232-253 (2011).
- [8] E. Candes, T. Tao, *Decoding by linear programming*, IEEE Trans. Inform. Theory, 51(12):4203-4215,2005.
- [9] E. Candes, J. Romberg, T. Tao, *Stable Signal Recovery from Incomplete and Inaccurate Measurements*, Comm. Pure Appl. Math., 59 (2006), pp. 1207-1223.
- [10] R. Chartrand, V. Staneva, *Restricted isometry properties and nonconvex compressive sensing*, Inverse Problems, 24(3):035020, 14 (2008).
- [11] S.S. Chen, D. L. Donoho, M. A. Saunders, *Atomic decomposition by basis pursuit*, SIAM J. Sci. Comput., 20(1):33-61,1998.
- [12] D. L. Donoho, *Compressed sensing*, IEEE TRans. Inform. Theory, 52(4):1289-1306,2006.
- [13] D. S. Dugdale, *Yielding of steel sheets containing slits*, J. Mech. Phys. Solids, 8 (1960), pp. 100-104.
- [14] V. Duval, G. Peyré, *Exact support recovery for sparse spikes deconvolution*, Found. Comput. Math., 15 (2015), pp. 1315-1355.
- [15] J. Fan, Y. Feng, Y. Wu, *Network exploration via the adaptive LASSO and SCAD penalties*, Ann. Appl. Stat., 3(2):521-541 (2009).
- [16] J. Fan, R. Li, *Variable selection via nonconcave penalized likelihood and its oracle properties*, J. Amer. Statist. Assoc., 96(456):1348-1360 (2001).

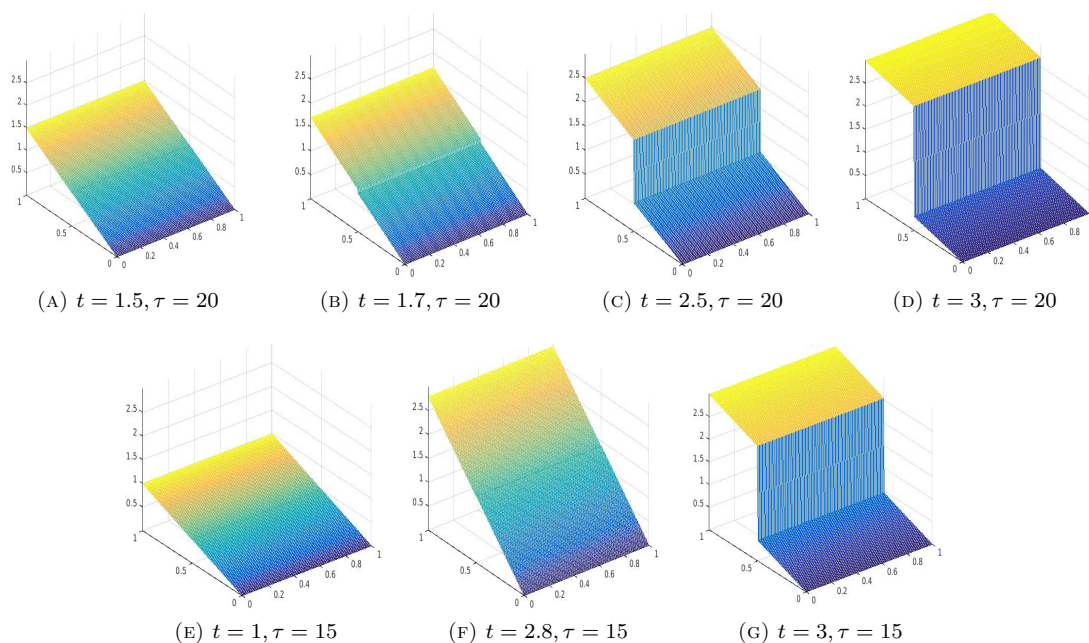


FIGURE 5. Displacement for the SCAD model, comparison between $\tau = 20$ and $\tau = 15$, $R^1 = R^2 = I$, boundary datum $g = g_1$.

- [17] J. Fan, H. Peng, Nonconcave penalized likelihood with a diverging number of parameters, *Ann. Statist.*, 32(3):928-961 (2004).
- [18] S. Foucart, M.-J. Lai, Sparsest solutions of underdetermined linear systems via ℓ_q -minimization for $0 < q \leq 1$, *Appl. Comput. Harmon. Anal.*, 26(3):395-407 (2009).
- [19] D. Ghilli, K. Kunisch, *A monotone scheme for sparsity optimization in ℓ^p with $p \in (0, 1]$* , to appear in IFAC WC 2017 Proceedings.
- [20] D. Ghilli, K. Kunisch, *On monotone and primal dual active set schemes for sparsity optimization in ℓ^p with $p \in (0, 1]$* , preprint 2017, arXiv:1709.06506.
- [21] P. Gong, C. Zang, Z. Lu, J. Z. Huang, J. Ye, *A general iterative shrinkage and thresholding algorithm for non-convex regularized optimization problems*, Proceeding ICML'13 Proceedings of the 30th International Conference on International Conference on Machine Learning-Volume 28, Pages II 37-II-45., Atlanta, GA, USA-June 16-21, 2013.
- [22] L. Gu, Y. Sheng, Y. Chen, H. Chang, Y. Zhang, P. Lv, W. Ji, T. Xu, *High-Density 3D single molecular analysis based on compressed sensing*, *Biophysical Journal*, 106 (2014), pp. 2443-2449.
- [23] S. T. Hess, T. P. Girirajan, M. D. Mason, *Ultra-high resolution imaging by fluorescence photoactivation localization microscopy*, *Biophysical Journal*, 91 (2006), pp. 4258-4272.
- [24] M. Hintermüller, Tao Wu, *Nonconvex TV^q -models in image restoration: analysis and a trust-region regularization-based superlinearly convergent solver*, *SIAM J. Imaging Sci.*, 6 (2013), pp. 1385-1415.
- [25] J. Huang, J. L. Horowitz, S. Ma, Asymptotic properties of bridge estimators in sparse high-dimensional regression models, *Ann. Statist.*, 26(2):587-613 (2008).
- [26] B. Huang, H. P. Babcock, X. Zhuang, *Breaking the diffraction barrier: super-resolution imaging of cells*, *Cell*, 143 (2010), pp. 1047-1058.
- [27] K. Ito, K. Kunisch, *A Variational approach to sparsity optimization based on Lagrange multiplier theory*, *Inverse Problems*, 30 (2014), 015001, 23pp.
- [28] Y. Jiao, B. Jin, X. Lu, *A primal dual active set with continuation algorithm for the ℓ^0 -regularized optimization problem*, *Appl. Comput. Harmon. Anal.*, 39 (2015), pp. 927-957.
- [29] Y. Jiao, B. Jin, X. Lu, W. Ren, *A primal dual active set algorithm for a class of nonconvex sparsity optimization*, Preprint, (2013).

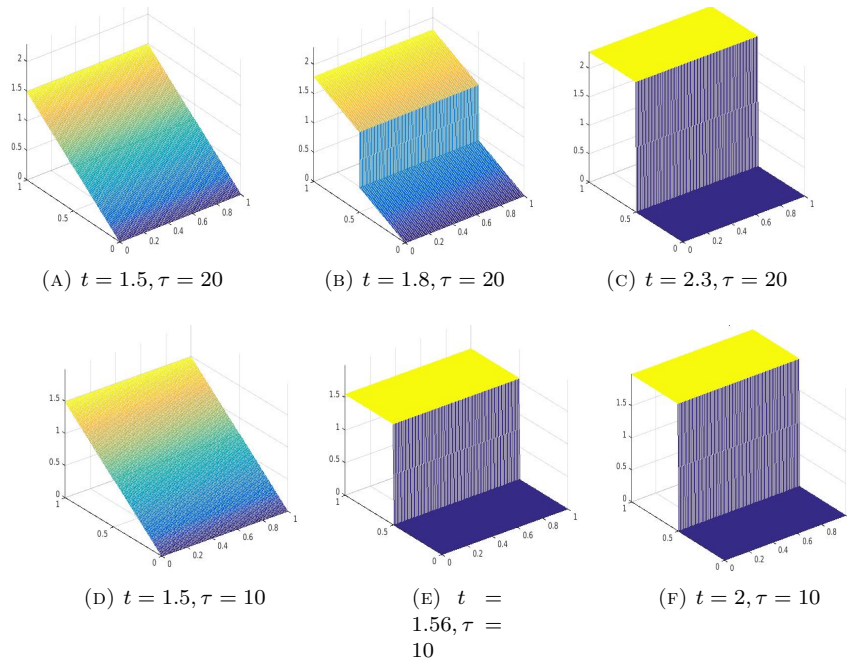


FIGURE 6. Displacement for the MCP model, comparison between $\tau = 20$ and $\tau = 10$, $R^1 = R^2 = I$, boundary datum $g = g_1$.

- [30] D. Kalise, K. Kunisch, Z. Rao, *Infinite horizon sparse optimal control*, J. Optim. Theory Appl., 172 (2017), pp. 481-517.
- [31] K. Knight, W. Fu, Asymptotics for lasso-type estimators, Ann. Statist., 28(5):1356-1378 (2000).
- [32] G. Li, T.K. Pong, *Global convergence of splitting methods for nonconvex composite optimization*, SIAM J. Optim., 25 (2014), pp. 2434-2460.
- [33] Q. Lyu, Z. Lin, Y. She, C. Zhang, *A comparison of typical ℓ^p minimization algorithms*, Neurocomputing 119 (2013), 413-424.
- [34] G. Del Piero, *A variational approach to fracture and other inelastic phenomena*, J. Elasticity, 112 (2013), pp. 3-77.
- [35] P. Ochs, A. Dosovitskiy, T. Brox, T. Pock, *On iteratively reweighted algorithms for nonsmooth nonconvex optimization in computer vision*, SIAM J. Imaging Sci., 8 (2015), pp. 331-372.
- [36] M. Rust, M. Bates, X. Zhuang, *Sub-diffraction-limit imaging by stochastic optical reconstruction microscopy (STORM)*, Nature Methods, 3 (2006), pp. 793-796.
- [37] Q. Sun, *Recovery of sparsest signals via ℓ^q -minimization*, Appl. Comput. Harmon. Anal., 32(3):329-341,2012.
- [38] D. Tuia, Rémi Flamary, Michel Barlaud, *Non-convex regularization in remote sensing*, IEEE Transactions on Geoscience and Remote Sensing, Institute of Electrical and Electronics Engineers, 2016.
- [39] R. Tibshirani, *Regression shrinkage and selection via the lasso*, J. Roy. Statist. Soc. Ser. B, 58(1):267-288,1996.
- [40] C.-H. Zhang, Nearly unbiased variable selection under minimax concave penalty, Ann. Statist., 38(2):894-942 (2010).
- [41] C.-H. Zhang, J. Huang, *The sparsity and bias of the LASSO selection in high-dimensional sparse estimation problems*, Statist. Sci, 27(4):576-593,2012.
- [42] L. Zhu, W. Zhang, D. Elnatan, B. Huang, *Faster STORM using compressed sensing*, Nature Methods, 9 (2012), pp. 721-723.

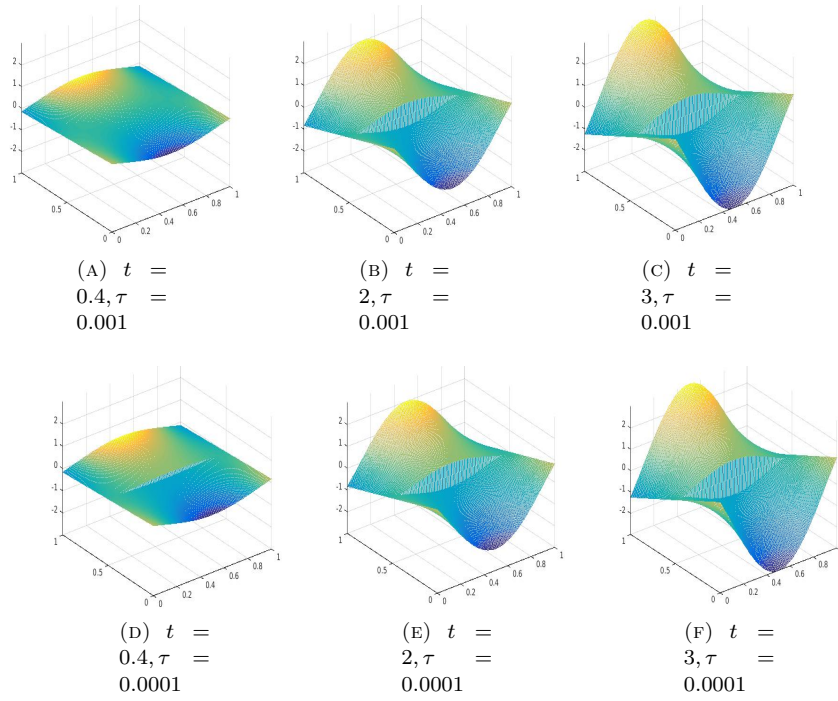


FIGURE 7. Displacement, $\theta(\cdot) = |\cdot|_{\tau}^{\tau}$, comparison between $\tau = 0.001$ and $\tau = 0.0001$, $R^1 = R^2 = I$, boundary datum $g = g_2$.

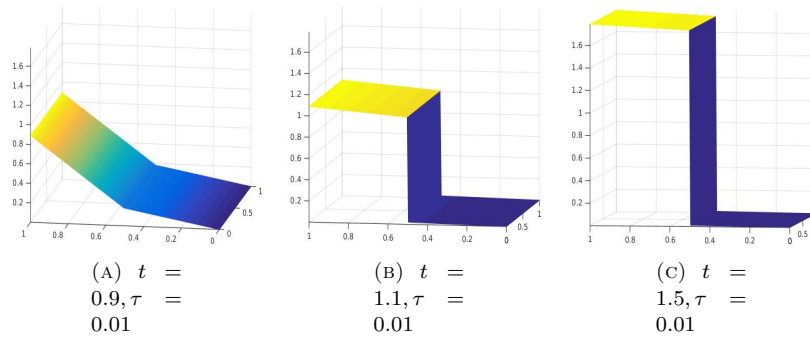


FIGURE 8. Displacement, $\theta(\cdot) = |\cdot|_{\tau}^{\tau}$, $\tau = 0.01$, R^1, R^2 given by (3.7)-(3.8), boundary datum $g = g_1$.

DARIA GHILLI, UNIVERSITY OF GRAZ, INSTITUTE OF MATHEMATICS AND SCIENTIFIC COMPUTING, UNIVERSITÄTSPLATZ 3, AUSTRIA

E-mail address: daria.ghilli@uni-graz.at

KARL KUNISCH, UNIVERSITY OF GRAZ, INSTITUTE OF MATHEMATICS AND SCIENTIFIC COMPUTING, UNIVERSITÄTSPLATZ 3, AUSTRIA, JOHANN RADON INSTITUTE FOR COMPUTATIONAL AND APPLIED MATHEMATICS (RICAM), AUSTRIAN ACADEMY OF SCIENCES, ALTENBERGERSTRASSE 69, LINZ, AUSTRIA,

E-mail address: karl.kunisch@uni-graz.at

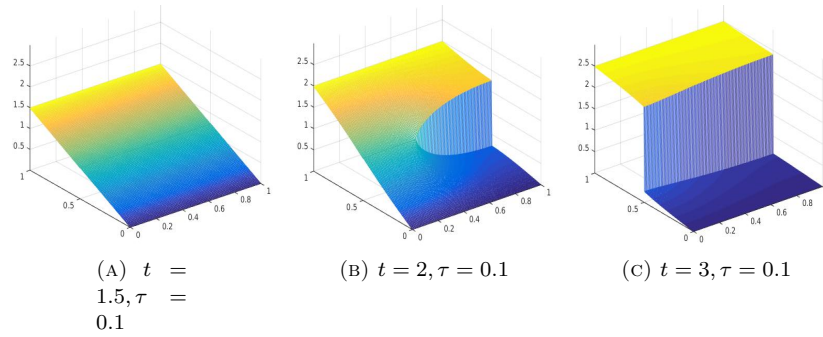


FIGURE 9. Displacement, $\theta(\cdot) = |\cdot|_{\tau}^{\tau}$, $\tau = 0.01$, R^1, R^2 given by (3.9), boundary datum $g = g_1$

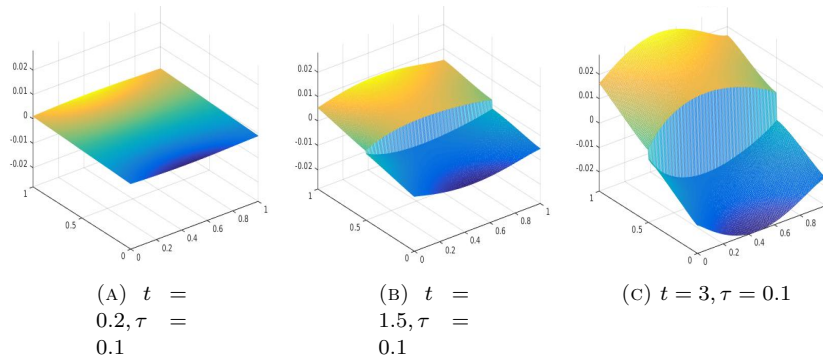


FIGURE 10. Displacement, $\theta(\cdot) = |\cdot|_{\tau}^{\tau}$, $\tau = 0.1$, R^1, R^2 given by (3.9), boundary datum $g = g_3$

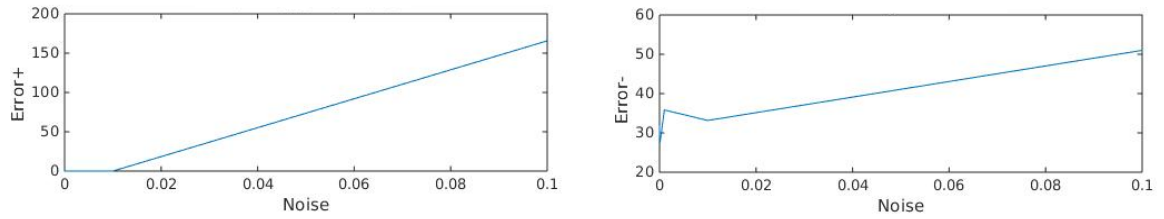


FIGURE 11. Error+ (surplus of emitters), Error- (missed emitters) against noise. Results obtained by **Algorithm 1**, $\tau = .5, \lambda = 10^{-6}$.

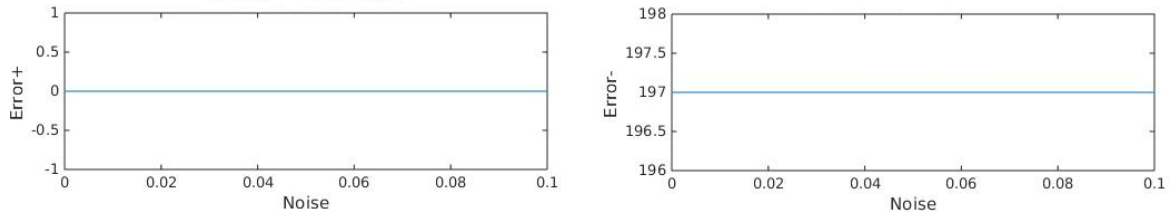


FIGURE 12. Error+ (surplus of emitters), Error- (missed emitters) against noise. Results obtained by GIST, $\tau = .5, \lambda = 10^{-6}$.

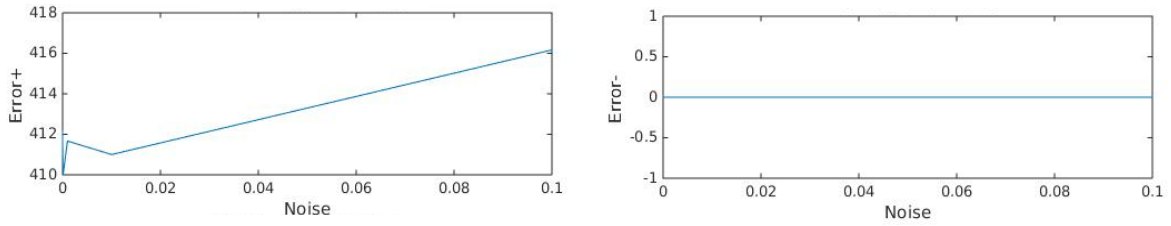


FIGURE 13. Error+ (surplus of emitters), Error- (missed emitters) against noise. Results obtained by the FISTA, $\lambda = 10^{-6}$.